

Electronic phase separation in iron pnictides

A. O. Sboychakov,^{1,2} A. V. Rozhkov,^{1,2} K. I. Kugel,^{1,2} A. L. Rakhmanov,^{1,2,3} and Franco Nori^{2,4}

¹*Institute for Theoretical and Applied Electrodynamics RAS, Moscow, 125412 Russia*

²*CEMS, RIKEN, Saitama, 351-0198, Japan*

³*Moscow Institute of Physics and Technology, Dolgoprudnyi, Moscow Region, 141700 Russia*

⁴*Department of Physics, University of Michigan, Ann Arbor, MI 48109-1040, USA*

(Dated: December 2, 2024)

A mechanism for electronic phase separation in iron pnictides is proposed. It is based on the competition between commensurate and incommensurate spin-density-wave phases in a system with an imperfect doping-dependent nesting of a multi-sheeted Fermi surface. We model the Fermi surface by two elliptical electron pockets and two circular hole pockets. The interaction between a carrier in a hole band and a carrier in an electron band leads to the formation of spin-density-wave order. The commensurate spin density wave in the parent compound transforms to the incommensurate phase when doping is introduced. We show that, for certain parameter values, the uniform state is unstable with respect to phase separation. The resulting inhomogeneous state consists of regions of commensurate and incommensurate spin-density-wave phases. Our results are in qualitative agreement with recent observations of incommensurate spin density waves and electronic inhomogeneity in iron pnictides.

PACS numbers: 64.75.Nx, 71.27.+a, 74.70.Xa

I. INTRODUCTION

Superconducting iron-based pnictides¹ attract considerable interest not only due to their high critical temperature, but also because of the rich physics of their electron subsystem. The phase diagram in iron pnictides contains areas of superconductivity, spin-density wave (SDW) order², both commensurate³ and incommensurate⁴, as well as the so-called orthorhombic phase⁵.

In addition, these materials frequently demonstrate charge inhomogeneity, exhibiting characteristic features of systems with electronic phase separation.^{2,6–10} The origin of this phase separation is important for understanding the mechanisms driving numerous phase transitions on the iron pnictides phase diagram.

The electronic inhomogeneity may be ascribed to sample imperfections and thus dismissed. However, another explanation to this phenomenon exists. Indeed, it has been known that the SDW ground state in a model with two spherical Fermi surfaces of unequal radius¹¹ can be unstable with respect to electronic phase separation^{12–14}. Variations of the latter model have been used to describe SDW in chromium¹¹ and graphene bilayer with AA stacking¹⁵. It is also analogous (but not identical) to the commonly used model of iron pnictides where one deals, roughly speaking, with elliptical rather than spherical electron and hole sheets of the Fermi surface. One can ask if a similar mechanism could apply to pnictides. In this paper, we demonstrate that the answer to this question is positive, and thus the charge inhomogeneity can result from a purely electronic mechanism. This finding is important for the interpretation of experimental data on charge inhomogeneity and for understanding the nature of the coexistence of the order parameters in iron pnictides.

For definiteness, we will focus here on iron pnictides,

although iron chalcogenides also exhibit phase separation.^{16,17} However, the physics related to the Fermi surface nesting may not be directly applicable to iron chalcogenides, especially to those containing alkaline atoms. Indeed, some chalcogenides do not have hole pockets, but nevertheless exhibit antiferromagnetism with rather high Néel temperatures.^{18–20} Moreover, the electron correlation effects in chalcogenides seem to be more pronounced than in pnictides.². Therefore, the case of iron chalcogenides requires a separate consideration.

This paper is organized as follows. In Sec. II we discuss the choice of the model Hamiltonian. Section III deals with the study of homogeneous SDW order in the mean-field approximation. The instability of the homogeneous state is proved in Sec. IV, where the phase diagram is constructed as well. The results are discussed in Sec. V.

II. MODEL

A. Kinetic energy

Unlike cuprates, which are believed to be in the strong electron-electron interaction regime, iron pnictides may be described by a weak-interaction model (see, e.g., discussion in Sec. IIIA of Ref. 21). In this approach the shape of the Fermi surface and the value of the Fermi velocity are the only relevant single-electron band parameters. The commonly used form of the Fermi surface for iron-based superconductors is shown schematically in Fig. 1(a).^{21–29} Here, we plot our Fermi surface within the first Brillouin zone, which corresponds to the square lattice of iron atoms, with one Fe atom per unit cell and the lattice constant a . Two quasi-two-dimensional nearly-circular hole pockets centered at the $\Gamma(0,0)$ point, and two elliptical-shaped electron pockets centered at

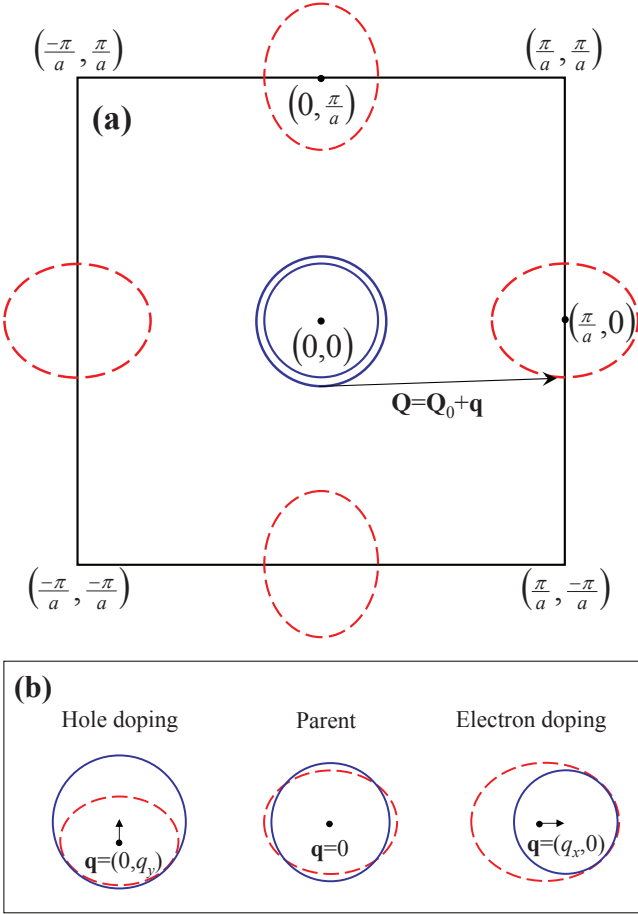


Figure 1: (Color online) (a) The Fermi surface of iron pnictides. Two circular hole pockets are centered around the $\Gamma(0,0)$ point, and two elliptic electron pockets are located near the $(0,\pi/a)$ and $(\pi/a,0)$ points. According to Ref. 22, only one hole and one electron band are involved in the formation of the SDW with a nesting vector $\mathbf{Q} = \mathbf{Q}_0 + \mathbf{q}$, where $\mathbf{Q}_0 = (\pi/a, 0)$, while two others remain untouched, giving rise to the metallic state for both the parent and the doped compound. (b) Fermi surface nesting at different doping levels for $\alpha > 0$: the electron pocket is shown shifted by the vector $-\mathbf{Q}$. For the parent compound $\mathbf{q} = 0$, while for the electron (hole) doping $x > 0$ ($x < 0$), the vector \mathbf{q} is parallel to the x axis (y axis), and $q_x(x) = q_y(-x)$ (see text).

the $M(0,\pi/a)$ and $M(\pi/a,0)$ points are taken into account. Less important parts of the Fermi surface are ignored. We will study a two-dimensional model, assuming that the interlayer electron tunneling and interactions are smaller than those inside the two-dimensional layers.

Thus, the Hamiltonian of the model has the form

$$H = H_0 + H_{\text{int}}, \quad (1)$$

where the kinetic energy term H_0 is given by

$$H_0 = \sum_{\mathbf{k}s\sigma} \varepsilon_{s\mathbf{k}}^h a_{\mathbf{k}s\sigma}^\dagger a_{\mathbf{k}s\sigma} + \sum_{\mathbf{k}s\sigma} \varepsilon_{s\mathbf{k}}^e b_{\mathbf{k}s\sigma}^\dagger b_{\mathbf{k}s\sigma}. \quad (2)$$

In this equation, $a_{\mathbf{k}s\sigma}^\dagger$, $a_{\mathbf{k}s\sigma}$ ($b_{\mathbf{k}s\sigma}^\dagger$, $b_{\mathbf{k}s\sigma}$) are the creation

and annihilation operators for electrons in the hole-like (electron-like) bands $s = 1, 2$ with the spectra $\varepsilon_{s\mathbf{k}}^h$ ($\varepsilon_{s\mathbf{k}}^e$).

To simplify our formalism, we assume that near the Fermi level the bands have quadratic dispersions. For the central circular hole-like bands we have ($\hbar = 1$)

$$\varepsilon_{1\mathbf{k}}^h = -\frac{v_F^h k^2}{2k_F} + \frac{v_F^h k_F}{2} - \mu, \quad (3)$$

$$\varepsilon_{2\mathbf{k}}^h = -\frac{v_F'^h k^2}{2k_F} + \frac{v_F'^h k_F}{2} - \Delta\epsilon - \mu. \quad (4)$$

where k_F is the Fermi momentum, μ is the chemical potential, v_F^h and $v_F'^h$ are the Fermi velocities for the hole bands. The energy shift $\Delta\epsilon$ in Eq. (3) defines the difference in radii of the two hole pockets: for $\Delta\epsilon > 0$ the radius of the second hole pocket is smaller than that of the first one.

As mentioned above, the electron components of the Fermi surface are elliptic. For these, the dispersion near the Fermi surface is given by the following relations:

$$\varepsilon_{1\mathbf{k}+\mathbf{Q}_0}^e = \varepsilon(k_x, k_y), \quad \varepsilon_{2\mathbf{k}+\mathbf{Q}'_0}^e = \varepsilon(k_y, k_x), \quad (5)$$

where the function ε is equal to

$$\varepsilon(k_x, k_y) = \frac{v_F^e k^2}{2k_F} - \frac{v_F^e k_F}{2} + \frac{\alpha v_F^e}{k_F} (k_y^2 - k_x^2) - \mu. \quad (6)$$

The centers of the elliptic bands are $\mathbf{Q}_0 = (\pi/a, 0)$ and $\mathbf{Q}'_0 = (0, \pi/a)$, and v_F^e is the Fermi velocity for the electron bands averaged over the Fermi surface. Note that in general $v_F^h \neq v_F'^h \neq v_F^e$. The chemical potential μ of the undoped compound is zero. The parameter α defines the ellipticity of the electron pockets. For the Fermi surface structure corresponding to Fig. 1(a), α is positive. In this case, the major axes of the ellipses are directed toward the Γ point. For $\alpha < 0$, the ellipses are rotated by 90° around their centers.

B. Interaction Hamiltonian

Due to the multi-sheeted structure of the Fermi surface, the interaction Hamiltonian H_{int} , in general, must include a number of terms describing interactions between carriers in different bands. However, since we are interested in the SDW order, most of these terms may be omitted for they do not contribute to the SDW phase transition¹¹. For this reason we ignore the electron-electron and hole-hole interactions.

It is known² that magnetic order in pnictides is “striped”. That is, the value of local magnetic moment oscillates along one of the crystal axes, remaining constant along the other axis. Such magnetic structure corresponds to the order parameter, which couples one of the hole bands (for definiteness, assume that it is the hole band ε_1^h) with one of the electron bands (assume that it is ε_1^e)²². The order parameter, which couples ε_1^h with both ε_1^e and ε_2^e , is unstable.²² Consequently, only

the interaction between ε_1^h and ε_1^e is crucial for the stabilization of the ordered phase. All other interaction terms will be discarded. We will re-examine this simplification in subsection III B [see discussion after Eq. (36)].

Keeping these considerations in mind, we split the model Hamiltonian into two parts, magnetic, H_m , and nonmagnetic (“reservoir”), H_r :

$$H = H_m + H_r, \quad (7)$$

$$H_m = \sum_{\mathbf{k}\sigma} \left[\varepsilon_{1\mathbf{k}}^h a_{\mathbf{k}1\sigma}^\dagger a_{\mathbf{k}1\sigma} + \varepsilon_{1\mathbf{k}}^e b_{\mathbf{k}1\sigma}^\dagger b_{\mathbf{k}1\sigma} \right] + \frac{V_1}{\mathcal{N}} \sum_{\mathbf{k}\mathbf{k}'\mathbf{K}\sigma\sigma'} a_{\mathbf{k}+\mathbf{K}1\sigma}^\dagger a_{\mathbf{k}1\sigma} b_{\mathbf{k}'-\mathbf{K}1\sigma'}^\dagger b_{\mathbf{k}'1\sigma'}, \quad (8)$$

$$H_r = \sum_{\mathbf{k}\sigma} \left[\varepsilon_{2\mathbf{k}}^h a_{\mathbf{k}2\sigma}^\dagger a_{\mathbf{k}2\sigma} + \varepsilon_{2\mathbf{k}}^e b_{\mathbf{k}2\sigma}^\dagger b_{\mathbf{k}2\sigma} \right]. \quad (9)$$

Here \mathcal{N} is the number of Fe atoms in a layer, $V_1 > 0$ is the coupling constant characterizing the Coulomb interaction between the bands $\varepsilon_{1\mathbf{k}}^h$ and $\varepsilon_{1\mathbf{k}}^e$. Below we will refer to these bands as magnetic bands. The bands $\varepsilon_{2\mathbf{k}}^h$ and $\varepsilon_{2\mathbf{k}}^e$ will be called nonmagnetic, since these do not contribute to the magnetic order parameter.

Model (7) is a generalization of the Rice model, proposed in Ref. 11 for the description of the incommensurate SDW order in chromium. The Hamiltonian of Ref. 11 has two bands, which participate in the magnetic transition, and a “reservoir” (nonmagnetic bands corresponding to H_r , where the subscript ‘r’ stand for “reservoir”). Unlike Eq. (7), the bands responsible for magnetic ordering in the Rice model have a spherical Fermi surface; therefore, at certain filling, the nesting is perfect.

III. INCOMMENSURATE SDW ORDER

A. Mean-field equations

We now consider the Hamiltonian (7) in the mean-field approximation. As we pointed out above, the Coulomb interaction in iron pnictides is weak, therefore, we assume below that

$$V_1/\varepsilon_F \ll 1, \quad (10)$$

where the Fermi energy ε_F is defined as

$$\varepsilon_F = \frac{v_F^e + v_F^h}{2} k_F \equiv v_F k_F. \quad (11)$$

The weak-coupling condition Eq. (10) guarantees the applicability of the mean-field approximation.

We will study the stability of the following SDW order parameter:

$$\Delta = \frac{V_1}{\mathcal{N}} \sum_{\mathbf{k}} \left\langle a_{\mathbf{k}1\uparrow}^\dagger b_{\mathbf{k}+\mathbf{Q}1\downarrow} \right\rangle = \frac{V_1}{\mathcal{N}} \sum_{\mathbf{k}} \left\langle a_{\mathbf{k}-\mathbf{q}1\uparrow}^\dagger b_{\mathbf{k}+\mathbf{Q}_01\downarrow} \right\rangle, \quad (12)$$

where the nesting vector \mathbf{Q} is equal to

$$\mathbf{Q} = \mathbf{Q}_0 + \mathbf{q}. \quad (13)$$

When $\mathbf{q} = 0$, our SDW is commensurate, whereas if \mathbf{q} is small, but non-zero, it is incommensurate. Other types of order parameter will be discussed in Sec. V.

The magnetization corresponding to the SDW order parameter Δ lies in xy plane. For the commensurate SDW case, in real space the “stripy” order is observed. Namely, the magnetization direction remains constant when one moves along the direction normal to \mathbf{Q}_0 . However, when one moves parallel to \mathbf{Q}_0 , the magnetization reverses its direction from one iron atom to the next iron atom. For incommensurate SDW, this “stripy” pattern slowly rotates in the xy plane: the local rotation angle $\phi(\mathbf{R})$ at the point \mathbf{R} is equal to $(\mathbf{q}\mathbf{R})$ [see panel (c) and (d) in Fig. 2].

In the mean-field approximation, the magnetic Hamiltonian Eq. (8) takes the form

$$H_m^{\text{MF}} = \sum_{\mathbf{k}\sigma} \left[\varepsilon_{1\mathbf{k}-\mathbf{q}}^h c_{\mathbf{k}\sigma}^\dagger c_{\mathbf{k}\sigma} + \varepsilon_{1\mathbf{k}+\mathbf{Q}_0}^e d_{\mathbf{k}\sigma}^\dagger d_{\mathbf{k}\sigma} \right. \\ \left. - \Delta \left(c_{\mathbf{k}\sigma}^\dagger d_{\mathbf{k}-\sigma} + d_{\mathbf{k}\sigma}^\dagger c_{\mathbf{k}-\sigma} \right) + \Delta^2/V_1 \right], \quad (14)$$

where we introduce the new operators $c_{\mathbf{k}\sigma}^\dagger = a_{\mathbf{k}-\mathbf{q}1\sigma}^\dagger$, $d_{\mathbf{k}\sigma}^\dagger = b_{\mathbf{k}+\mathbf{Q}_01\sigma}^\dagger$, and Δ is assumed to be real. The Hamiltonian Eq. (14) can be easily diagonalized. The quasiparticle energies are

$$E_{\mathbf{k}}^{(1,2)} = \frac{\varepsilon_{1\mathbf{k}+\mathbf{Q}_0}^e + \varepsilon_{1\mathbf{k}-\mathbf{q}}^h}{2} \mp \sqrt{\Delta^2 + \frac{1}{4} \left(\varepsilon_{1\mathbf{k}+\mathbf{Q}_0}^e - \varepsilon_{1\mathbf{k}-\mathbf{q}}^h \right)^2}. \quad (15)$$

The grand potential Ω_m (per one Fe atom) corresponding to H_m^{MF} is ($k_B = 1$)

$$\Omega_m = -2T \sum_s \int_{BZ} \frac{v_0 d^2 \mathbf{k}}{(2\pi)^2} \ln \left[1 + e^{-E_{\mathbf{k}}^{(s)}/T} \right] + \frac{2\Delta^2}{V_1}, \quad (16)$$

where v_0 is the volume of the unit cell, and the integration is performed over the 2D Brillouin zone. The SDW gap Δ and the nesting vector \mathbf{Q} are found from the minimization of Ω_m

$$\frac{\partial \Omega_m}{\partial \Delta} = 0, \quad \frac{\partial \Omega_m}{\partial \mathbf{q}} = 0. \quad (17)$$

It will be shown below that in the weak-coupling limit Eq. (10), the SDW order can exist only if the deviation from the perfect nesting is small, that is:

$$|\alpha| \ll 1. \quad (18)$$

In addition, the gap Δ is small compared to ε_F , and the deviation \mathbf{q} of the nesting vector \mathbf{Q} from the commensurate value \mathbf{Q}_0 is also small

$$|\mathbf{q}| = |\mathbf{Q} - \mathbf{Q}_0| \sim \Delta/v_F \ll k_F. \quad (19)$$

Restricting ourselves to the limit of zero temperature, we can write the first of Eqs. (17) in the following form

$$1 = \frac{V_1}{2} \int \frac{v_0 d^2 \mathbf{k}}{(2\pi)^2} \frac{1 - \Theta(E_{\mathbf{k}}^{(1)}) - \Theta(-E_{\mathbf{k}}^{(2)})}{\sqrt{\Delta^2 + \frac{1}{4} (\varepsilon_{1\mathbf{k}+\mathbf{Q}_0}^e - \varepsilon_{1\mathbf{k}-\mathbf{q}}^h)^2}}, \quad (20)$$

where $\Theta(x)$ is the step function.

When the lower band $E_{\mathbf{k}}^{(1)}$ is filled, while the upper band $E_{\mathbf{k}}^{(2)}$ is empty, the gap attains its maximum value Δ_0 . In this case, $\Theta(E_{\mathbf{k}}^{(1)}) = \Theta(-E_{\mathbf{k}}^{(2)}) = 0$ for any \mathbf{k} , and Eq. (20) becomes

$$1 = \frac{V_1}{2} \int dE \frac{\bar{\rho}(E)}{\sqrt{\Delta_0^2 + E^2}}, \quad (21)$$

where the generalized density of states is defined as

$$\bar{\rho}(E) = \int \frac{v_0 d^2 \mathbf{k}}{(2\pi)^2} \delta \left(E - \frac{\varepsilon_{1\mathbf{k}+\mathbf{Q}_0}^e - \varepsilon_{1\mathbf{k}}^h}{2} \right). \quad (22)$$

Evaluating $\bar{\rho}(E)$ we set $\mathbf{q} = 0$, since taking into account values of the order of $|\mathbf{q}| \sim \Delta/v_F$ gives only second-order corrections in Eq. (21).

If $|E| \ll \varepsilon_F$, the function $\bar{\rho}(E)$ can be calculated explicitly using Eqs. (3) and (5) for the band spectra $\varepsilon_{1\mathbf{k}+\mathbf{Q}_0}^e$ and $\varepsilon_{1\mathbf{k}}^h$. As a result, near the Fermi surface we obtain

$$\bar{\rho}(E) \approx \bar{\rho}(0) = \frac{v_0 k_F^2}{2\pi \varepsilon_F}, \quad |E| \ll \varepsilon_F. \quad (23)$$

When the energy E is of the order of the band width, $\bar{\rho}(E)$ vanishes. This makes the integral in Eq. (21) convergent, and one can derive the usual BCS-like expression for the gap:

$$\Delta_0 \approx \varepsilon_F \exp \left(-\frac{2\pi \varepsilon_F}{v_0 k_F^2 V_1} \right). \quad (24)$$

If the sample is doped, then $E_{\mathbf{k}}^{(1)} > 0$ or $E_{\mathbf{k}}^{(2)} < 0$ for some range of \mathbf{k} , and the equation for the band gap becomes

$$\ln \frac{\Delta_0}{\Delta} = \int \frac{\varepsilon_F d^2 \mathbf{k}}{4\pi k_F^2} \frac{\Theta(E_{\mathbf{k}}^{(1)}) + \Theta(-E_{\mathbf{k}}^{(2)})}{\sqrt{\Delta^2 + \frac{1}{4} (\varepsilon_{1\mathbf{k}+\mathbf{Q}_0}^e - \varepsilon_{1\mathbf{k}-\mathbf{q}}^h)^2}}. \quad (25)$$

Substituting Eqs. (3) and (5) into Eq. (25), and taking into account Eqs. (18) and (19), after straightforward algebra we derive the equation for the band gap in the form

$$\ln \frac{1}{\delta} = \int \frac{d\varphi}{2\pi} \operatorname{Re} \left\{ \cosh^{-1} \left[\frac{\nu_0(\mathbf{p}, \varphi) - \nu}{\delta} \right] \right\}, \quad (26)$$

where,

$$\nu_0(\mathbf{p}, \varphi) = p_x \cos \varphi + p_y \sin \varphi - \frac{\bar{\alpha}}{2} \cos 2\varphi, \quad (27)$$

$$\bar{\alpha} = \frac{\alpha \varkappa \varepsilon_F}{\Delta_0}, \quad (28)$$

and we introduce the following dimensionless quantities

$$\varkappa = \frac{2\sqrt{v_F^e v_F^h}}{v_F^e + v_F^h}, \quad \delta = \frac{\Delta}{\Delta_0}, \quad \nu = \frac{\mu}{\varkappa \Delta_0}, \quad \mathbf{p} = \frac{\varkappa v_F \mathbf{q}}{2\Delta_0}. \quad (29)$$

Transforming similarly the second of Eqs. (17), we obtain the equation for the nesting vector $\mathbf{Q} = \mathbf{Q}_0 + 2\Delta_0 \mathbf{p}/v_F \varkappa$,

$$\begin{pmatrix} p_x \\ p_y \end{pmatrix} = \int_0^{2\pi} \frac{d\varphi}{\pi} \begin{pmatrix} \cos \varphi \\ \sin \varphi \end{pmatrix} \operatorname{sgn}(\nu_0(\mathbf{p}, \varphi) - \nu) \times \operatorname{Re} \sqrt{(\nu_0(\mathbf{p}, \varphi) - \nu)^2 - \delta^2}. \quad (30)$$

Equations (26) and (30) determine the SDW band gap Δ and the nesting vector \mathbf{Q} as functions of μ . However, experiments are performed at fixed doping, not chemical potential. Thus, we have to relate the electron density and μ . The total number of electrons per iron atom, $n(\mu)$, is the sum of the number of electrons in the nonmagnetic and the magnetic bands: $n(\mu) = n_r(\mu) + n_m(\mu)$, where

$$\begin{aligned} n_r(\mu) &= \frac{2}{N} \sum_{\mathbf{k}} [\Theta(-\varepsilon_{2\mathbf{k}}^h) + \Theta(-\varepsilon_{2\mathbf{k}}^e)], \\ n_m(\mu) &= -\frac{\partial \Omega_m}{\partial \mu}. \end{aligned} \quad (31)$$

The doping is defined by

$$x(\mu) = n(\mu) - n(0). \quad (32)$$

Performing calculations similar to those described above, we obtain for the doping level

$$\begin{aligned} \frac{x}{x_0} &= r\nu - \int_0^{2\pi} \frac{d\varphi}{2\pi} \operatorname{sgn}(\nu_0(\mathbf{p}, \varphi) - \nu) \times \\ &\quad \operatorname{Re} \sqrt{(\nu_0(\mathbf{p}, \varphi) - \nu)^2 - \delta^2}, \end{aligned} \quad (33)$$

where

$$x_0 = \frac{2v_0 k_F^2 \Delta_0}{\pi \varkappa \varepsilon_F}, \quad r = \frac{\varkappa^2}{\varkappa'^2}, \quad \varkappa' = \frac{2\sqrt{v_F^e v_F^h}}{v_F^e + v_F^h}. \quad (34)$$

The first (second) term in Eq. (33) is the nonmagnetic (magnetic) contribution x_r (x_m) to the total doping x . Equations (26), (30), and (33) form a closed system of equations for the self-consistent determination of $\Delta(x)$, $\mathbf{Q}(x)$, and $\mu(x)$.

B. Results: Homogeneous state

Our numerical analysis reveals that Eq. (26) has no solutions if $|\bar{\alpha}| > 2.0$. Thus, the equality $|\bar{\alpha}| = 2.0$ determines the critical value of the ellipticity parameter α_c : for a given coupling constant V_1 , the SDW ordering occurs only if

$$|\alpha| < \alpha_c = \frac{2\Delta_0}{\varkappa\varepsilon_F}. \quad (35)$$

Conversely, this condition Eq. (35) may be re-formulated as a requirement on the interaction strength: for given band parameters (α , \varkappa , etc.) the SDW is stable only if

$$V_1 > V_c = \frac{2\pi\varepsilon_F}{v_0 k_F^2 \ln \frac{2}{|\alpha|\varkappa}}. \quad (36)$$

Equation (36) allows us to re-examine the assumption we made in subsection II B. When constructing the interaction Hamiltonian, we discarded several terms including the interaction between electrons in $\varepsilon_{1,2}^e$ and holes in the second hole band ε_2^h . When mapping the phase diagram, Eq. (36) is very useful since it assures that a sufficiently weak interaction does not affect the phase diagram: to induce a new ordered phase, the corresponding coupling constant must exceed V_c . Since the ordering of the second hole band is not observed experimentally, we conclude that the pertinent interaction is too weak, and, consequently, may be neglected.

It is seen from Eqs. (29) and (34) that the parameter \varkappa only renormalizes the dimensionless quantities ν , \mathbf{p} , and x_0 . Thus, at fixed $\bar{\alpha}$ and r , it is enough to know the functions $\Delta(x)$, $\mathbf{q}(x)$, and $\mu(x)$ for $\varkappa = 1$. For $\varkappa \neq 1$ these functions are found by simple rescaling as $\Delta(x\varkappa)$, $\mathbf{q}(x\varkappa)/\varkappa$, and $\varkappa\mu(x\varkappa)$. For this reason, below we study only the $\varkappa = 1$ case. Note that, typically, for a real material all Fermi velocities are of the same order, thus $\varkappa \sim 1$.

The computed functions $\Delta(x)$ and $q(x)$ are shown in Fig. 2(a) and (b) for $r = \varkappa = 1$ and two different values of $\bar{\alpha}$. At low doping, $|x| < x_1^*$, where the critical doping x_1^* depends on model parameters, all the extra charge goes to the nonmagnetic bands. As a result, the order parameter is independent of x , $\Delta(x) = \Delta_0$, $\mathbf{q}(x) = 0$, and the chemical potential increases linearly with x ,

$$\mu(x) = \frac{\Delta_0 x}{rx_0}. \quad (37)$$

In such a regime, the system shows commensurate SDW order.

When $|x| = x_1^*$, the chemical potential touches the bottom (top) of the upper (lower) magnetic band. Upon further doping, electrons (holes) appear in the band $E_{\mathbf{k}}^{(2)}$ ($E_{\mathbf{k}}^{(1)}$). The SDW order becomes incommensurate,³⁰ $\mathbf{q} \neq 0$. The order of the transition into the incommensurate state depends on the parameters $\bar{\alpha}$ and r . If $r < r_1 \approx$

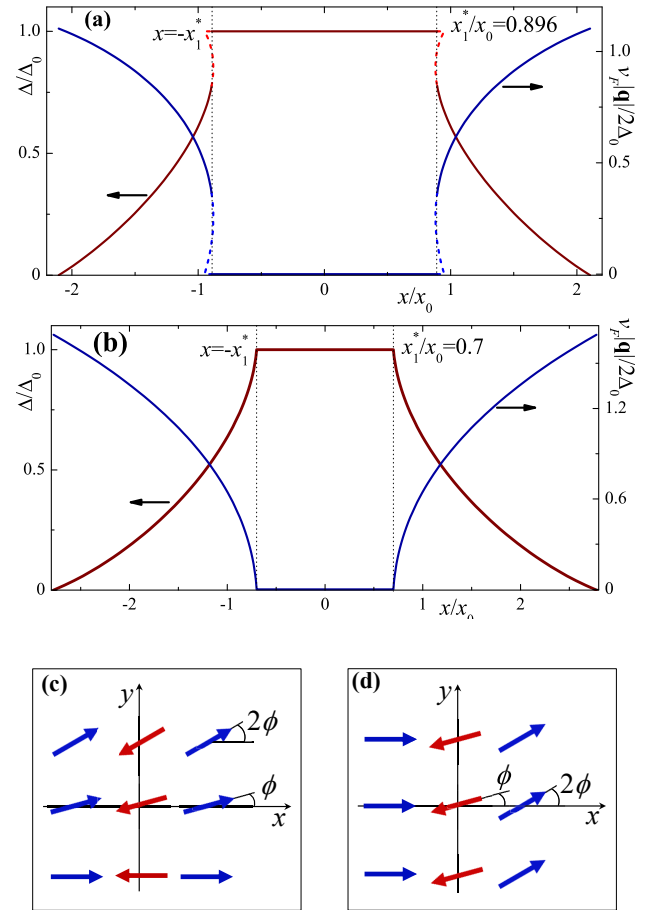


Figure 2: (Color online) Dependence of the normalized order parameter Δ/Δ_0 and wave vector $|\mathbf{q}|$ on the doping x , for $r = \varkappa = 1$. (a) Here $\bar{\alpha} = 0.1$. The transition from commensurate to incommensurate SDW state is of first order: both Δ and $|\mathbf{q}|$ abruptly change at $x = x_1^*$. The dashed curves show the functions $\Delta(x)$ and $|\mathbf{q}(x)|$ corresponding to the metastable state. (b) Here $\bar{\alpha} = 0.6$. The transition from commensurate to incommensurate SDW state is now of second order. Panels (c) and (d) show schematics of the incommensurate SDW spin structure. If $\alpha > 0$, then panel (c) corresponds to hole doping ($x < 0$) and (d) to electron doping ($x > 0$). If $\alpha < 0$, then panel (c) corresponds to electron doping, while panel (d) corresponds to hole doping.

0.38, the transition is of second order for any $\bar{\alpha}$, while for larger r it becomes of first order if $|\bar{\alpha}| < \bar{\alpha}_1(r)$. In the case of first-order transitions, both Δ and $|\mathbf{q}|$ abruptly change at $x = x_1^*$, see Fig. 2(a).

Electron doping ($x > 0$) is in many respects similar to hole doping ($x < 0$). Indeed, the functions $\Delta(x)$, $\mu(x)$, and $|\mathbf{q}(x)|$ obey particle-hole symmetry relations:

$$\Delta(-x) = \Delta(x), \quad (38)$$

$$\mu(-x) = -\mu(x), \quad (39)$$

$$|\mathbf{q}(-x)| = |\mathbf{q}(x)|. \quad (40)$$

In addition, these functions are independent of the sign of α . However, the direction of the vector $\mathbf{q}(x)$ depends on

the sign of α and on the type of doping. When $\alpha > 0$, the vector $\mathbf{q}(x)$ is parallel to the x axis for electron doping and to the y axis for hole doping. The direction of $\mathbf{q}(x)$ is reversed if $\alpha < 0$. Thus, the nesting vector $\mathbf{Q} = (Q_x, Q_y)$ is given by the following formulas

$$Q_x = \frac{\pi}{a} + \frac{2\Delta_0 p(|x|)}{\varkappa v_F}, \quad Q_y = 0, \quad \text{if } \alpha x > 0, \quad (41)$$

$$Q_x = \frac{\pi}{a}, \quad Q_y = \frac{2\Delta_0 p(|x|)}{\varkappa v_F}, \quad \text{if } \alpha x < 0. \quad (42)$$

How does the incommensurate SDW described by these equations look like in real space? Let us introduce the integer-valued vector $\mathbf{n} = (n, m)$. Then the position of a given iron atom is equal to $\mathbf{R}_n = a\mathbf{n}$. For the order parameter Δ , Eq. (12), the SDW magnetization vector lies in the xy plane: $S_n^z = 0$. The in-plane components can then be expressed as:

$$\mathbf{S}_n = S_0 \left(\cos(a\mathbf{Q} \cdot \mathbf{n}), \sin(a\mathbf{Q} \cdot \mathbf{n}) \right), \quad (43)$$

where $S_0 = \Delta/V_1$. Thus, we obtain

$$\mathbf{S}_n = S_0 \begin{cases} (-1)^n (\cos \phi n, \sin \phi n), & \alpha x > 0, \\ (-1)^n (\cos \phi m, \sin \phi m), & \alpha x < 0, \end{cases} \quad (44)$$

where $\phi = a|\mathbf{q}|$. These spin configurations are schematically shown in Fig. 2 (c) and (d) for hole and electron doping, respectively. For positive (negative) α , panel (c) corresponds to $x > 0$ ($x < 0$), and panel (b) corresponds to $x < 0$ ($x > 0$).

IV. PHASE SEPARATION

In the previous section we assumed that the ground state of the model is homogeneous. Here we demonstrate that there is a part of the phase diagram where homogeneous states are not stable, and the true ground state is phase separated. To detect this instability, the chemical potential must be calculated.

The computed dependence of the chemical potential μ on doping x is shown in Fig. 3 for three different values of $\bar{\alpha}$ and $r = \varkappa = 1$ for electron doping ($x > 0$). The dependence $\mu(x)$ for hole doping can be easily determined using particle-hole symmetry, as discussed in the previous section.

The function $\mu(x)$ shown on Fig. 3 demonstrates several peculiar features in the vicinity of the commensurate-incommensurate phase transition point x_1^* . Specifically, for low $\bar{\alpha}$, the function $\mu(x)$ is non-monotonic and multi-valued near $x \approx x_1^*$ [see Fig. 3(a)]. At higher $\bar{\alpha}$, the multivaluedness disappears; however, the non-monotonicity remains [see Fig. 3(b)]. This vanishes at even higher values of $\bar{\alpha}$ [as in Fig. 3(c)].

We now observe that in Fig. 3(a) and Fig. 3(b) there are finite ranges of doping, where the chemical potential decreases as the doping increases. This means that the

compressibility of the electronic system is negative and the homogeneous state is unstable with respect to separation into two phases³¹. The phase transitions between homogeneous commensurate and incommensurate SDW phases, which we described in subsection III B, will be masked, at least partially, by the phase separation.

In the separated state there exist two phases, phase 1 and phase 2, with electron density $x_1 (< x_1^*)$ and $x_2 (> x_1^*)$, and with the volume fractions p_1 and p_2 satisfying the conditions $p_1 + p_2 = 1$ and $x_1 p_1 + x_2 p_2 = x$. As one can see from Fig. 3 (a,b), the phase 1 is the commensurate and the phase 2 is the incommensurate SDW state. The concentrations x_1 and x_2 are found from the equations³¹ $\mu(x_1) = \mu(x_2) \equiv \mu_0$ and $\Omega_1 = \Omega_2$, where $\Omega_{1,2}$ are grand potentials in the phases 1 and 2. The latter condition means the equality of two shaded areas shown in Fig. 3(a,b) (the so-called Maxwell construction).

The range of doping x , where the phase separation exists, is largest when $\alpha = 0$. In this case our model is identical to the two-dimensional Rice model¹¹, for which the presence of the phase separation was shown in Refs. 12,13. The range of the phase separation, $x_1 < x < x_2$, shrinks if $|\bar{\alpha}|$ increases, and disappears at the critical value $\bar{\alpha}_c \cong 1.15$. The phase separated state does not exist for $|\bar{\alpha}| > \bar{\alpha}_c$.

The results obtained are summarized in the phase diagram in the $(x, \bar{\alpha})$ plane shown in Fig. 4. This phase diagram is calculated for $r = \varkappa = 1$. It remains qualitatively the same if $r \neq 0$. If the nonmagnetic bands are absent, $r = 0$, the homogeneous commensurate SDW phase exists only when $x = 0$. Consequently, the electronic concentration x_1 in the phase 1 is zero in the phase separated state for any $\bar{\alpha}$.

Finally, we would like to draw the attention of the reader to an unexpected feature of the phase diagram in Fig. 4. Namely, the second order incommensurate SDW-to-paramagnet transition line bends to the right, while all other transition lines on the phase diagram bend to the left. In other words, the value of doping where the transition from paramagnetic to incommensurate SDW phase occurs increases when the ellipticity parameter α increases. Interpreting this feature, however, one must keep in mind that the nesting quality is controlled not only by α but also by μ (or x). The parameter α controls the shape of the electron pocket, while μ (or doping) controls the relative areas of electron and hole pockets. Therefore, at larger doping levels, when the areas of the electron and hole pockets differ substantially, the electron and hole pockets could be better nested for larger ellipticity of the electron pocket.

V. DISCUSSION

The most important result obtained here is the prediction of electronic phase separation in some range of doping. The separated phase consists of a mixture of commensurate and incommensurate SDW phases with

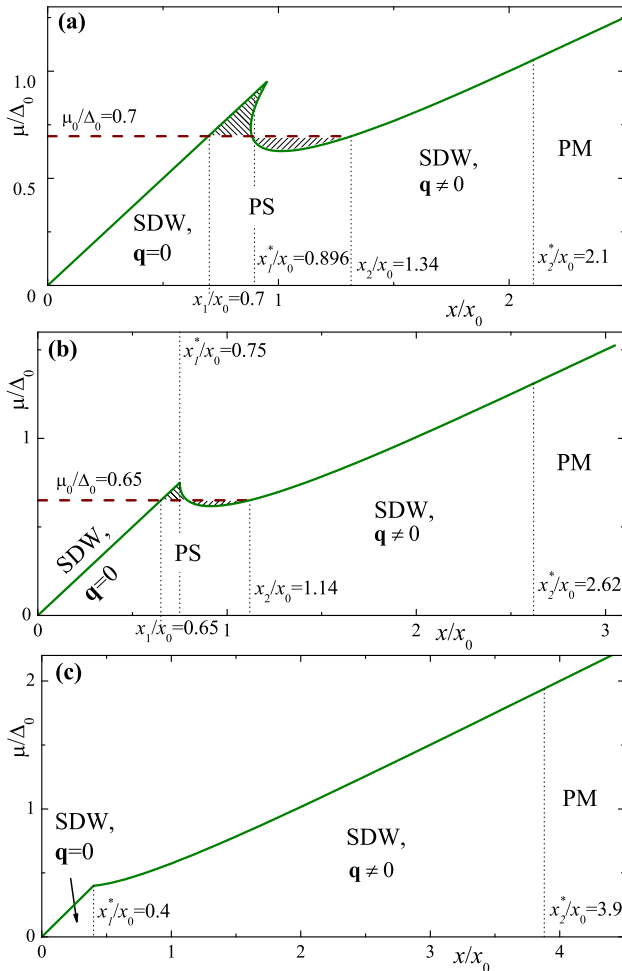


Figure 3: (Color online) Chemical potential $\mu(x)$ calculated at $\bar{\alpha} = 0.1$ (a), $\bar{\alpha} = 0.5$ (b), and $\bar{\alpha} = 1.2$ (c). Here, $r = \varkappa = 1$. (a) and (b): the homogeneous state is unstable toward phase separation if $x_1 < x < x_2$. The dashed (red) curve corresponds to the μ_0 found using the Maxwell construction. The shaded areas above and below μ_0 are equal to each other. (c): $\mu(x)$ monotonically increases with x , no phase separation appears. The homogeneous commensurate ($\mathbf{q} = 0$) and incommensurate ($\mathbf{q} \neq 0$) SDW, paramagnetic (PM), and inhomogeneous commensurate–incommensurate SDW (PS) states are separated by vertical dotted lines.

different electronic concentrations. The phase separation in iron-based superconductors was observed in several experiments^{6–9}. For example, the inhomogeneous state with a commensurate antiferromagnetic and non-magnetic domains with characteristic sizes ~ 65 nm was observed in the hole doped $\text{Ba}_{1-x}\text{K}_x\text{Fe}_2\text{As}_2$ compound.⁶ Our theory predicts that the second phase is the incommensurate SDW rather than a nonmagnetic one. However, the proposed mechanism of phase separation can, in general, be consistent with the observations reported in Ref. 6. We found that the thermodynamic potentials of the incommensurate SDW and the metastable paramagnetic phases are very close to each other in the doping

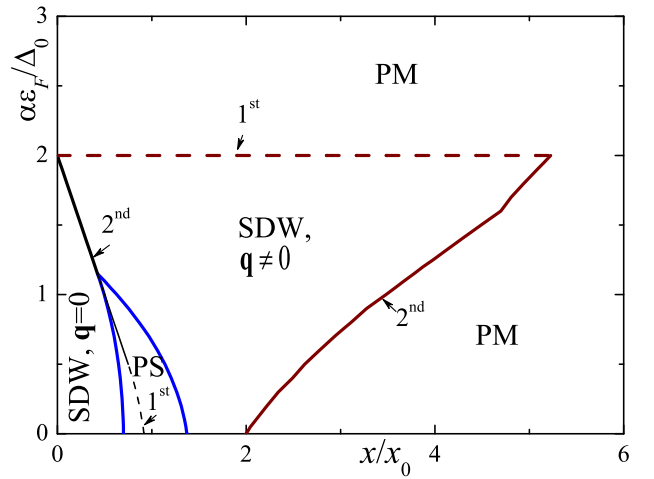


Figure 4: (Color online) The phase diagram of the model (7) in the $(x, \bar{\alpha})$ plane; for $r = \varkappa = 1$ and $\alpha, x > 0$. It is symmetric with respect to the replacement $x \rightarrow -x$ and/or $\alpha \rightarrow -\alpha$. The boundary between incommensurate SDW and paramagnetic (PM) states shown by the dashed (red) curve corresponds to the first order and by the solid (red) curve to the second order phase transition. Solid (blue) lines indicate the boundaries of the phase separated (PS) state. The solid (black) curve (second order transition) and dashed (black) curve (first order transition) show the boundaries between commensurate ($\mathbf{q} = 0$) and incommensurate ($\mathbf{q} \neq 0$) homogeneous SDW phases. Note that phase separation partially masks the transition line between the homogeneous SDW states.

range $x > x_2$. The incommensurate SDW phase can be destroyed by an additional reason not taken into account in our model, e.g., by disorder. In this case the phase separation might occur between the commensurate SDW and the paramagnetic phases. In addition, the incommensurate SDW order parameter may be difficult to detect due to its weakness.

The geometry of the emergent inhomogeneities and their characteristic sizes are beyond the scope of the present study. The electron concentrations in separated phases are different; hence, the inhomogeneities are charged and one should take into consideration the electrostatic contribution to the total energy. The characteristic sizes of the inhomogeneities are controlled by the interplay between the long-range Coulomb interaction and the energy of the surface between the phases. In the simplest case, the structure of the inhomogeneous state corresponds to the droplets of one phase embedded in the matrix of another phase. However, depending on the properties of the system, other geometries are possible, such as alternating layers of different phases, stripes, etc.^{32–35} When disorder is present in the sample, it also affects the structure of the inhomogeneous phase.

In our study we chose the order parameter Δ , Eq. (12). In the literature, a different order parameter is also discussed.^{12,36} This order parameter is not homogeneous: SDW gap experiences periodic modulations in real space.

When the state with such an order parameter is doped, the extra charges go to the places where the gap locally vanishes. The latter type of order may be more stable than Eq. (12). However, for several reasons we decided to avoid such an option. Specifically, analytical calculations with inhomogeneous gap become very complicated. Further, the choice of the order parameter affects somewhat the phase diagram and, in particular, the region of the phase separation; however, the inhomogeneous region does not disappear. In addition, we must remember that the relative stability of different order parameters is likely a non-universal quantity, which depends on a variety of microscopic parameters (e.g., details of the band structure, interaction, disorder). Therefore, the type of suitable order parameter cannot be deduced without input from experiments.

It follows from the phase diagram in Fig. 4 that the smaller effective ellipticity parameter $\bar{\alpha}$, the larger the region of the phase separation. The SDW gap Δ_0 increases with increasing coupling potential V_1 . Therefore, a stronger coupling is more favorable for phase separation since $\bar{\alpha} \propto \alpha/\Delta_0$ [see Eq. (28)].

Our mean-field approach is not applicable in the limit of strong coupling, where the use of Hubbard-like models is more appropriate. The phase separation in such models is a common phenomenon^{37–45}. Thus, we expect that the existence of phase separation in our model is not an exclusive feature of the weak-coupling regime.

The model studied here predicts an incommensurate SDW phase for both electron and hole doping in the range of dopant concentrations scaled by the parameter x_0 , Eq. (34). From the latter equation we conclude that $x_0 \ll 1$ if the weak-coupling condition, Eq. (10), is met. Thus, we predict the existence of the incommensurate SDW order for small doping, $x \ll 1$.

The incommensurate SDW phase is characterized by the vector $\mathbf{q} = \mathbf{Q} - \mathbf{Q}_0$. Our calculations show that there are only two possible equilibrium directions of \mathbf{q} : it can be either parallel, or perpendicular to \mathbf{Q}_0 , depending on the type of doping and the sign of the ellipticity parameter α [see Eqs. (41) and (42)]. It is clear, however, that both the magnitude and direction of \mathbf{q} is sensitive to the shape of the Fermi surface, which is simplified in the present calculations. In real materials, the shape of the hole pockets deviates from perfect circles. Moreover, the spectrum of the hole and electron bands depend on the transverse momentum, k_z , which is completely neglected in the model considered here. In particular, the electron bands have corrugated structure^{46,47}, that is, the major axis of the ellipses are rotated by 90° when k_z varies from

0 to π . Nevertheless, we believe that the model studied here captures the main features of the incommensurate SDW state in pnictides.

Indeed, the observation of the incommensurate SDW phase with \mathbf{q} perpendicular to \mathbf{Q}_0 in the electron doped $\text{Ba}(\text{Fe}_{1-x}\text{Co}_x)_2\text{As}_2$ was recently reported in Ref. 4. The measured value of $|\mathbf{q}|$ was about 0.02–0.03 for the concentration range $0.056 < x < 0.06$. Such values of x and \mathbf{q} , as well as the direction of \mathbf{q} (corresponding to $\alpha < 0$), are consistent with our theory.

The short-range incommensurate SDW phase was described in Ref. 48 for the electron doped $\text{BaFe}_{2-x}\text{Ni}_x\text{As}_2$. In general, one must be cautious interpreting this experiment using our model, since the observed short-range SDW correlations do not correspond to our long-range SDW order. However, we note that the measured vector \mathbf{q} was perpendicular to \mathbf{Q}_0 , which is also consistent with a negative α .

We found no experimental work reporting the observation of the incommensurate SDW phase in the hole-doped pnictides. However, double-peaked spin fluctuations at $\mathbf{Q} = \mathbf{Q}_0 \pm \mathbf{q}$ have been observed^{49,50} in the hole-doped $\text{Ba}_{1-x}\text{K}_x\text{Fe}_2\text{As}_2$ compound in a wide doping range. In these measurements^{49,50} the vector \mathbf{q} was found to be parallel to \mathbf{Q}_0 , which, again, corresponds to $\alpha < 0$ in our model.

In conclusion, we study a model with imperfect nesting of the Fermi surface suitable for the description of iron pnictides. We show that the incommensurate SDW phase arises in the system at a finite doping level. We demonstrate that two spin configurations can arise in the system depending on the model parameters. It was shown that the homogeneous state is unstable toward phase separation into commensurate and incommensurate SDW phases in a specific doping range. These results are in qualitative agreement with the recent experimental observation of the incommensurate SDW order and phase separation in doped superconducting pnictides.

Acknowledgments

The work was supported by ARO, Grant-in-Aid for Scientific Research (S), MEXT Kakenhi on Quantum Cybernetics, the JSPS via its FIRST program, and by the Russian Foundation for Basic Research (projects 11-02-00708, 11-02-00741, 12-02-92100-JSPS, and 12-02-00339). A.O.S. acknowledges support from the RFBR project 12-02-31400 and the Dynasty Foundation.

¹ Y. Kamihara, T. Watanabe, M. Hirano, and H. Hosono, *J. Am. Chem. Soc.* **130**, 3296 (2008).

² P. Dai, J. Hu, and E. Dagotto, *Nature Phys.* **8**, 709 (2012).

³ J. Dong, H.J. Zhang, G. Xu, Z. Li, G. Li, W.Z. Hu, D. Wu, G.F. Chen, X. Dai, J.L. Luo, Z. Fang and N.L. Wang,

EPL **83**, 27006 (2008).

⁴ D.K. Pratt, M.G. Kim, A. Kreyssig, Y.B. Lee, G.S. Tucker, A. Thaler, W. Tian, J.L. Zarestky, S.L. Budko, P.C. Canfield, B.N. Harmon, A.I. Goldman, and R. J. McQueeney, *Phys. Rev. Lett.* **106**, 257001 (2011).

⁵ C. de la Cruz, Q. Huang, J.W. Lynn, J. Li, W. Ratcliff II, J.L. Zarestky, H.A. Mook, G.F. Chen, J.L. Luo, N.L. Wang, P. Dai, *Nature* **453**, 899 (2008); T. Nomura, S.W Kim, Y. Kamihara, M. Hirano, P.V. Sushko, K. Kato, M. Takata, A.L. Shluger, and H. Hosono, *Supercond. Sci. Technol.* **21**, 125028 (2008).

⁶ J.T. Park, D.S. Inosov, Ch. Niedermayer, G.L. Sun, D. Haug, N.B. Christensen, R. Dinnebier, A.V. Boris, A.J. Drew, L. Schulz, T. Shapoval, U. Wolff, V. Neu, X. Yang, C.T. Lin, B. Keimer, and V. Hinkov, *Phys. Rev. Lett.* **102**, 117006 (2009).

⁷ D.S. Inosov, A. Leineweber, X. Yang, J.T. Park, N.B. Christensen, R. Dinnebier, G.L. Sun, Ch. Niedermayer, D. Haug, P.W. Stephens, J. Stahn, O. Khvostikova, C.T. Lin, O.K. Andersen, B. Keimer, and V. Hinkov, *Phys. Rev. B* **79**, 224503 (2009).

⁸ G. Lang, H.-J. Grafe, D. Paar, F. Hammerath, K. Mauthay, G. Behr, J. Werner, and B. Büchner, *Phys. Rev. Lett.* **104**, 097001 (2010).

⁹ B. Shen, B. Zeng, G.F. Chen, J.B. He, D.M. Wang, H. Yang and H.H. Wen, *EPL* **96**, 37010 (2011).

¹⁰ Q. Luo, G. Martins, D.-X. Yao, M. Daghofer, R. Yu, A. Moreo, and E. Dagotto, *Phys. Rev. B* **82**, 104508 (2010).

¹¹ T.M. Rice, *Phys. Rev. B* **2**, 3619 (1970).

¹² A.A. Gorbatsevich, Yu.V. Kopaev, I.V. Tokatly, *Zh. Eksp. Teor. Fiz.* **101**, 971 (1992) [Sov. Phys. JETP **74**, 521 (1992)].

¹³ A.L. Rakhmanov, A.V. Rozhkov, A.O. Sboychakov, and F. Nori, *Phys. Rev. B* **87**, 075128 (2013).

¹⁴ A.L. Rakhmanov, A.V. Rozhkov, A.O. Sboychakov, and F. Nori, *Phys. Rev. B* **87**, 121401(R) (2013).

¹⁵ A.L. Rakhmanov, A.V. Rozhkov, A.O. Sboychakov, and F. Nori, *Phys. Rev. Lett.* **109**, 206801 (2012).

¹⁶ A. Ricci, N. Poccia, G. Campi, B. Joseph, G. Arrighetti, L. Barba, M. Reynolds, M. Burghammer, H. Takeya, Y. Mizuguchi, Y. Takano, M. Colapietro, N.L. Saini, and A. Bianconi, *Phys. Rev. B* **84**, 060511(R) (2011).

¹⁷ A. Ricci, N. Poccia, B. Joseph, G. Arrighetti, L. Barba, J. Plaisier, G. Campi, Y. Mizuguchi, H. Takeya, Y. Takano, N.L. Saini, and A. Bianconi, *Supercond. Sci. Technol.* **24**, 082002 (2011).

¹⁸ X.-P. Wang, T. Qian, P. Richard, P. Zhang, J. Dong, H.-D. Wang, C.-H. Dong, M.-H. Fang and H. Ding, *EPL* **93**, 57001 (2011).

¹⁹ Y. Zhang, *Nature Mater.* **10**, 273 (2011).

²⁰ D. Mou, Sh. Liu, X. Jia, J. He, Y. Peng, L. Zhao, Li Yu, G. Liu, Sh. He, X. Dong, J. Zhang, H. Wang, Ch. Dong, M. Fang, X. Wang, Q. Peng, Zh. Wang, Sh. Zhang, F. Yang, Z. Xu, Ch. Chen, and X.J. Zhou *Phys. Rev. Lett.* **106**, 107001 (2011).

²¹ G.R. Stewart, *Rev. Mod. Phys.* **83**, 1589 (2011).

²² I. Eremin and A.V. Chubukov, *Phys. Rev. B* **81**, 024511 (2010).

²³ S. Raghu, X.-L. Qi, Ch.-X. Liu, D.J. Scalapino, and S.-C. Zhang, *Phys. Rev. B* **77**, 220503 (2008).

²⁴ M. Daghofer, A. Moreo, J.A. Riera, E. Arrigoni, D.J. Scalapino, and E. Dagotto, *Phys. Rev. Lett.* **101**, 237004 (2008).

²⁵ M. Daghofer, A. Nicholson, A. Moreo, and E. Dagotto, *Phys. Rev. B* **81**, 014511 (2010).

²⁶ J. Hu and N. Hao, *Phys. Rev. X* **2**, 021009 (2012).

²⁷ P. Richard, T. Sato, K. Nakayama, T. Takahashi, and H. Ding, *Rep. Prog. Phys.* **74**, 124512 (2011).

²⁸ M.J. Calderón, B. Valenzuela, and E. Bascones, *Phys. Rev. B* **80**, 094531 (2009).

²⁹ J. Fink, S. Thirupathaiah, R. Ovsyannikov, H.A. Dürr, R. Follath, Y. Huang, S. de Jong, M.S. Golden, Y.-Zh. Zhang, H.O. Jeschke, R. Valentí, C. Felser, S. Dastjani Farahani, M. Rotter, and D. Johrendt, *Phys. Rev. B* **79**, 155118 (2009).

³⁰ A. B. Vorontsov, M.G. Vavilov, and A.V. Chubukov, *Phys. Rev. B* **79**, 060508(R) (2009); *ibid.*, **81**, 174538 (2010).

³¹ M. Le Bellac, F. Mortessagne, and G.G. Batrouni, *Equilibrium and Non-Equilibrium Statistical Thermodynamics*, (Cambridge Univ. Press, Cambridge 2004).

³² J. Lorenzana, C. Castellani, and C. Di Castro, *Phys. Rev. B* **64**, 235127, 235128 (2001).

³³ R. Jamei, S. Kivelson, and B. Spivak, *Phys. Rev. Lett.* **94**, 056805 (2005).

³⁴ C. Ortix, J. Lorenzana, and C. Di Castro, *Phys. Rev. Lett.* **100**, 246402 (2008).

³⁵ K.I. Kugel, A.L. Rakhmanov, A.O. Sboychakov, F.V. Kusmartsev, N. Poccia, and A. Bianconi, *Supercond. Sci. Tech.* **22**, 014007 (2009).

³⁶ L.P. Gor'kov, G.B. Teitel'baum, *Phys. Rev. B* **82**, 020510(R) (2010).

³⁷ E. Dagotto, *Nanoscale Phase Separation and Colossal Magnetoresistance: The Physics of Manganites and Related Compounds* (Springer-Verlag, Berlin, 2003).

³⁸ E. Nagaev, *Colossal Magnetoresistance and Phase Separation in Magnetic Semiconductors* (Imperial College Press, London, 2002).

³⁹ M.Yu. Kagan and K.I. Kugel, *Usp. Fiz. Nauk.* **171**, 577 (2001) [Physics - Uspekhi **44**, 553 (2001)].

⁴⁰ G.C. Milward, M.J. Calderon, and P.B. Littlewood, *Nature* **433**, 607 (2005).

⁴¹ E. Dagotto, *New J. Phys.* **7**, 67 (2005).

⁴² N.B. Ivanova, S.G. Ovchinnikov, M.M. Korshunov, I.M. Eremin, and N. V. Kazak, *Usp. Fiz. Nauk.* **179**, 837 (2009) [Physics - Uspekhi **52**, 789 (2009)].

⁴³ K.I. Kugel, A.L. Rakhmanov, and A.O. Sboychakov, *Phys. Rev. Lett.* **95**, 267210 (2005).

⁴⁴ E. Dagotto, *Science* **309**, 257 (2005).

⁴⁵ A.O. Sboychakov, K.I. Kugel, and A.L. Rakhmanov, *Phys. Rev. B* **76**, 195113 (2007).

⁴⁶ S. Graser, A.F. Kemper, T.A. Maier, H.-P. Cheng, P.J. Hirschfeld, and D.J. Scalapino, *Phys. Rev. B* **81**, 214503 (2010).

⁴⁷ V. Brouet, M.F. Jensen, P.-H. Lin, A. Taleb-Ibrahimi, P. Le Fèvre, F. Bertran, Ch.-H. Lin, W. Ku, A. Forget, and D. Colson, *Phys. Rev. B* **86**, 075123 (2012).

⁴⁸ H. Luo, R. Zhang, M. Laver, Z. Yamani, M. Wang, X. Lu, M. Wang, Y. Chen, Sh. Li, S. Chang, J.W. Lynn, and P. Dai, *Phys. Rev. Lett.* **108**, 247002 (2012).

⁴⁹ C.H. Lee, K. Kihou, H. Kawano-Furukawa, T. Saito, A. Iyo, H. Eisaki, H. Fukazawa, Y. Kohori, K. Suzuki, H. Usui, K. Kuroki, and K. Yamada, *Phys. Rev. Lett.* **106**, 067003 (2011).

⁵⁰ J.-P. Castellan, S. Rosenkranz, E.A. Goremychkin, D.Y. Chung, I.S. Todorov, M.G. Kanatzidis, I. Eremin, J. Knolle, A.V. Chubukov, S. Maiti, M.R. Norman, F. Weber, H. Claus, T. Guidi, R.I. Bewley, and R. Osborn, *Phys. Rev. Lett.* **107**, 177003 (2011).